Nanoscale

PAPER

View Article Online
View Journal | View Issue

Cite this: *Nanoscale*, 2025, **17**, 12758

$Ti_3C_2T_x$ MXene augments osmo-adaptive repression of the inflammatory stress response for improved wound repair†

Sertan Kiziloz,‡[a] Emma J. Ward,‡[a] Daniel Hawthorne,[a] Avick Sinha,[a,b] Grace Cooksley,[c] Dipak Sarker,[a] Cyril Crua,[d] Andrew Lloyd,[a] Christopher E. Shuck,[e] Yury Gogotsi[f] and Susan Sandeman *[a]

Chronic non-healing wounds represent a growing global health challenge that is poorly addressed by current advances in wound care dressings. Hyperosmotic stress linked, for example, to poor glycaemic control, is a known but under-investigated contributor to the chronic wound environment and a known inflammatory stimulus. MXene ($Ti_3C_2T_x$) has been considered for smart dressing applications but has not been investigated for use with bioactive agents to directly moderate hyperosmotic stress for improved wound care. In this study, $Ti_3C_2T_x$, in combination with osmolyte betaine, was used to investigate hyperosmotic stress-induced effects on wound closure. The effect of these materials was measured using a wound closure scratch assay, and data was used to mathematically model changes in HaCaT human keratocyte migratory rate and velocity. Changes in the upregulation of apoptotic and inflammatory markers were measured, and qualitative changes in phalloidin-labelled actin cytoskeletal structure were observed. A *tert*-butyl glycine betainate (*t*Bu-GB) polyacrylate microgel loaded $Ti_3C_2T_x$ dressing was then fabricated and tested for biocompatibility and slow elution of osmolyte over time. Osmotic stress at levels that did not induce cell death reduced the migratory capacity of keratocytes to close the scratch. Migration by osmotically stressed keratocytes was reduced by more than 50% at 24 h and remained at 65% (±5%) at 48 h compared to complete scratch closure at 24 h in the cell only control. This reduction was reversed by a $Ti_3C_2T_x$ coating, allowing complete scratch closure by 48 h in the osmotically stressed group. Exposure of osmotically stressed cells to betaine increased normalised wound closure in the osmotically stressed keraotycte group at each time point and this was augmented by the presence of a $Ti_3C_2T_x$ coating. Osmotic stress induced upregulation of inflammatory markers IL-6, IL-1α, IL-1β, CXCL1, and CXCL8 by at least 10-fold. The effect was significantly greater in the presence of bacterial LPS and this was significantly reduced by the presence of $Ti_3C_2T_x$ alone and in combination with betaine. Sustained and slow release of betaine was demonstrated from a *t*Bu-GB-microgel loaded $Ti_3C_2T_x$ dressing over 48 h supporting the use of such dressings to improve osmotic stress induced, poor wound closure rates.

Received 5th November 2024,
Accepted 10th April 2025

DOI: 10.1039/d4nr04622f

rsc.li/nanoscale

1. Introduction

Advances in nanomaterials for wound repair have yet to significantly impact the growing global clinical health challenge of chronic non-healing wounds. In the UK alone, an estimated 3.8 million patients receive treatment for chronic wounds at an estimated cost of £5.6 billion.[1] A partial explanation lies in the complexity of non-healing wounds and the impact of co-morbidities, such as diabetes, which can negatively influence the success of targeted treatments.[2,3] An underexplored aspect of this challenge is the role of osmotic imbalance in delayed wound repair and potential strategies to address it using bioactive wound dressings.[4,5] A promising, relatively new class of transition metal carbides, nitrides, and carbonitrides, called

[a]*Centre for Regenerative Medicine and Devices, School of Applied Sciences, University of Brighton, Brighton BN2 4GJ, UK. E-mail: s.sandeman@brighton.ac.uk*
[b]*Advanced Engineering Centre, University of Brighton, Brighton BN2 4GJ, UK*
[c]*Developmental Biology and Cancer (DBC) Research and Teaching Department, UCL GOS Institute of Child Health, London WC1N 1EH, UK*
[d]*School of Engineering and Informatics, University of Sussex, Brighton, BN1 9QJ, UK*
[e]*Department of Chemistry and Chemical Biology, Rutgers University, Piscataway, NJ 08854, USA*
[f]*Department of Materials Science and Engineering and A. J. Drexel Nanomaterials Institute, Drexel University, Philadelphia, PA 19104, USA*
†Electronic supplementary information (ESI) available. See DOI: https://doi.org/10.1039/d4nr04622f
‡Joint first authors.

MXenes, have recently been used within a smart dressing application.[6] However, MXenes have yet to be considered in combination with other bioactive agents to moderate hyperosmotic stress and stimulate a shift beyond a chronic hyper-inflammatory state to wound resolution.

The chronic wound, though complex, is defined by several parameters. It remains stalled in the inflammatory stage beyond 12 weeks rather than progressing through the classic stages of normal wound repair, moving from haemostasis, inflammation and proliferation to remodelling.[7–9] The wound bed tends to be characterised by increased reactive oxygen species, inflammatory cytokines, matrix metalloprotease (MMP), lysozyme and other protease activity, fibroblast senescence, increased pH, increased tendency to infection, increased glucose concentration in the case of diabetes, delayed angiogenesis and delayed proliferative re-epithelialisation.[10,11] A key challenge is to address the impact of local and systemic factors that maintain prolonged and dysregulated inflammation rather than progressing sequentially through the stages of wound repair to close the wound. Bioactive dressings synthesised with materials that aim to adaptively respond to changes in the wound bed and release active drugs or molecules to enable improved wound repair are a promising approach to improve treatment.[12] However, combination materials that allow slow payload release into the wound bed, potentially using biological signals (*e.g.*, MMPs, lysozyme or other proteases, pH, temperature, reactive oxygen species) from the wound bed, have yet to be effectively utilised.

Developments beyond basic gauze dressings provide an array of available routes for chronic wound care. Advanced dressings, acting by physical and chemical means, include films, foams, hydrocolloids, and hydrogels and tend to be selected based on the presence of infection, moisture control, and requirements to remove excess wound exudate where necessary.[13,14] However, evidence indicating the benefits of one dressing over another for chronic wound closure is limited.[14] Additional therapeutic options have been considered, incorporating both non-cellular and cellular, biologically active components.[12,15,16] These include biopolymers and nanomaterials within the dressing which are responsive to changes in the wound bed as well as regenerative factors which can be slowly eluted into the wound bed following triggered release. Examples include the use of growth factors to promote wound closure and neovascularisation,[17] antimicrobial peptides (AMPs) to target infection associated delays in wound repair,[18,19] collagen/mesenchymal stem cell combinations to modulate macrophage behaviour and stimulate skin flap repair,[20,21] and the use of silver nanoparticles as antibacterial and anti-inflammatory dressing components.[22,23] However, major challenges exist in the application of these approaches. For example, AMP-loaded systems must maintain the stability of the AMP on variations in the wound environment such as temperature and pH in addition to improved, selective toxicity towards bacterial cells only.[19–21] Stem cell therapies face limitations to efficacy based on challenges in preparation and delivery. The intensively studied silver nanoparticles face challenges on repeated and prolonged use due to tissue accumulation and toxicity.[22,24] Whilst investigated bioactives show benefits for aspects of wound bed pathophysiology issues such as manufacturing complexity, cost, stability, regulatory requirements, sensitivity to degradation, and potential destruction by the immune system remain.[5] In addition, methods by which bioactive agents can be protected from the harsh wound bed environment for controlled and sustained efficacy remain an open challenge.

$Ti_3C_2T_x$ MXenes are inflammation-repressive nanomaterials,[25,26] and have been used as sensor materials for dermal applications and within dressings to improve wound healing.[6] $Ti_3C_2T_x$ is synthesised through selective chemical etching of the Ti_3AlC_2, MAX phase, precursor and follows the general formula, $M_{n+1}X_nT_x$, where M represents the early transition metal, titanium, X is carbon, and T refers to surface functional groups, typically –O, –OH, or –F. Useful properties in a biomedical context include biocompatibility, flexibility, metallic electrical conductivity, hydrophilicity, and tuneable surface chemistry, making these highly versatile materials.[25,27,28] Extensive reviews have highlighted the potential of MXenes in the wound dressing field and the need for refinement for optimisation of current approaches.[29] Here, we propose their use in combination with an encapsulated osmolyte to anchor the hydrophilic osmolyte to $Ti_3C_2T_x$ and the wound dressing for slow and sustained elution over time into the wound bed.

Osmolytes are part of the osmo-adaptive response, which exists physiologically to control tissue osmolarity and maintain an osmotic environment conducive to normal cell function.[30] Among the osmolytes endogenous to mammals, glycine betaine (GB) is the most well characterised as the primary osmoprotectant utilised to restore osmotic balance in key tissues including those of the kidneys, heart, liver, and brain.[31–36] It is synthesised endogenously in humans *via* oxidation of choline in addition to exogenous dietary sources.[37] Topical application of GB, at concentrations of 2–200 mM, has been shown to increase resistance to osmotic stress in corneal tissue in addition to modulation of epidermal tight junctional barrier function for subsequently improved skin wound repair.[38–41] On exposure to a hyperosmotic environment, osmolytes are synthesised and taken up by cells to protect protein and DNA function, stabilise the intracellular environment, and prevent water efflux.[42] However, pathological variations in osmotic control result in cell shrinkage through dehydration, cytoskeletal damage, protein and DNA disruption, cell cycle arrest, and apoptosis.[42] Such shifts in osmotic control can occur within the wound bed microenvironment, particularly in chronic conditions such as diabetes, where raised glucose levels alter cell capacity for osmo-adaptive control and a normal wound healing response.[2,11] The goal of the current study is, therefore, to improve cell resilience and address osmotic imbalance for resolution of the chronic non-healing wound using a microencapsulated osmoprotectant/$Ti_3C_2T_x$ combination materials approach. It is hypothesised that $Ti_3C_2T_x$, in combination with a well-studied osmoprotec-

tant GB, will significantly improve sustained wound repair characteristics, repress hyper-inflammatory stimulus and improve the potential for wound closure.

2. Experimental

2.1. Synthesis and spray-coating of $Ti_3C_2T_x$

$Ti_3C_2T_x$ was synthesised using the minimally intensive layer delamination (MILD) method,[43] etching MAX phase (Ti_3AlC_2; synthesis conditions described in previous literature[44]) and delaminating to yield single flake $Ti_3C_2T_x$. Continuous stirring of 9 M hydrochloric acid (20 mL) (Sigma Aldrich, UK), 1.6 g lithium fluoride (Sigma Aldrich, UK), and 1 g Ti_3AlC_2 at 35–40 °C was carried out for 24 h. The synthesised sediment was resuspended in 50 mL deionised (DI) water and centrifuged (ALC PK 120R Centrifuge, DJB Labcare Ltd, UK) at 2191*g* for 5 min. The sediment was resuspended, and the centrifugation/wash step was repeated until pH 6 was achieved. The sediment was stirred with 1 g lithium chloride (Sigma Aldrich, UK), for 4 h to improve delamination yield. The centrifugation/wash step was repeated to achieve pH 6 again, and the supernatant was collected. The supernatant was then centrifuged further at a higher speed of 14 000*g* for 10 min to isolate the delaminated $Ti_3C_2T_x$ flakes. The resultant sediment from the final centrifugation step was resuspended in DI water and stored at −20 °C before use.

A 12-well tissue culture plate was spray-coated with $Ti_3C_2T_x$ at a concentration of 5 mg mL^{-1}. The tissue culture plate was mounted on a clamp stand, and the spray gun nozzle was 15 cm away from the plate. The plate was covered with parafilm, only exposing the relevant wells for spray-coating of the appropriate amount per well.

2.2. Characterisation of $Ti_3C_2T_x$ and $Ti_3C_2T_x$ coatings

2.2.1. UV-Vis spectroscopy. A known volume of synthesised $Ti_3C_2T_x$ was vacuum filtered, dried, and weighed to determine its gravimetric concentration. From the known concentration, a series of dilutions from 1 : 16, 1 : 8, 1 : 4 to 1 : 2 were prepared. Absorbance was measured by UV-Vis spectrometry (UV 2401-PC, SHIMADZU Ltd, UK) using a wavelength range of 200 to 1000 nm and an optical path length of 1 cm.

2.2.2. Dynamic light scattering analysis. Dynamic light scattering (DLS) (Zetasizer Nano Series Pro Red, Malvern USA) was used to measure the particle size dispersity at a 90° scattering angle. 5 μL of the $Ti_3C_2T_x$ neat colloidal solution was diluted in 1 mL of DI water and the particle size was calculated, averaging five measurements per sample.

2.2.3. X-ray diffraction. X-ray diffraction (XRD) (Rigaku Miniflex X-ray Diffractometer, USA) was performed on $Ti_3C_2T_x$ dry film and powdered Ti_3AlC_2 using a Cu K_α radiation source (λ = 1.5406 Å) at 40 kV and a 15 nA beam current. Patterns were collected with a 0.01° 2θ angular count interval on a rotating stage at 10 rpm.

2.2.4. Contact angle analysis. $Ti_3C_2T_x$ coating surface hydrophilicity was assessed using the sessile drop contact angle method. 5 μL of DI water was deposited onto $Ti_3C_2T_x$ spray-coated and uncoated glass slides. Contact angle measurements were taken using an OCA 15EC contact angle device and analysed using SCA 20 software (DataPhysics Instruments GmbH, Germany).

2.3. Assessing the osmoprotective effects of GB-$Ti_3C_2T_x$ using an *in vitro* HaCaT model of wound repair

2.3.1. Cell culture. Immortalised human keratocyte cells (HaCaTs) (AddexBio, UK) were cultured in Dulbecco's Modified Eagle Medium (DMEM) (Thermofisher Scientific, UK), supplemented with 10% foetal bovine serum (FBS) (Thermofisher Scientific, UK) at 37 °C, 5% CO_2. Cells were passaged on reaching 80% confluency by standard trypsinisation.

2.3.2. Scratch assay to measure the effect of GB-$Ti_3C_2T_x$ on HaCaT cell migration. The effect of $Ti_3C_2T_x$ and GB on the ability of osmotically stressed keratocytes to migrate across a scratch was measured using a cell migration scratch assay. A 12-well tissue culture plate was spray-coated with 5 mg mL^{-1} $Ti_3C_2T_x$ and UV-sterilised for 2 h. HaCaT cells were seeded onto $Ti_3C_2T_x$ coated plates and uncoated control plates at a seeding density of 5×10^5 cells per mL and incubated at 37 °C, 5% CO_2 for 24 h. The media was aspirated off and a scratch was drawn vertically across the plate. The wells were washed with phosphate buffered saline (PBS) and the treatments were then added to the cells following dilution in culture media. Conditions included untreated cell-only control, bacterial lipopolysaccharide (LPS) treated (5 μg mL^{-1}) (Thermofisher Scientific, UK), mannitol-treated (550 mOsM) (Sigma Aldrich, UK), mannitol LPS treated, mannitol and glycine betaine (GB) (10 mM) treated (Sigma Aldrich, UK), and mannitol with GB and LPS treated cells. Each condition was prepared in duplicate. Images were captured by light microscopy (Carl Zeiss Microscope GmbH, Germany) at time points of 0, 4, 8, 12, 24, 36, 48 h.

2.3.3. Cell migration rate and velocity modelling. A modified Tabatabai growth model for wound closure percentage (WC),[45] was used to assess the impact of $Ti_3C_2T_x$ and GB on scratch cell edge closure rate under normal and hyperosmotic conditions in the presence and absence of LPS. WC was calculated according to eqn (1).

$$\mathrm{WC} = \frac{M}{\left(\left(1 + \frac{M}{a}\right)e^{(-(b\cdot T)-(c\cdot a\ \sinh(t)))}\right)} \quad (1)$$

In this equation, M represents the maximum potential closure percentage, while the coefficient α corresponds to the reference size from the curve fit, ensuring dimensional consistency. The variable t denotes time in hours, tracking the progression of wound closure. Parameters b and c influence the closure rate, with b affecting the initial exponential increase and c controlling the hyperbolic sine function $a\sinh(t)$. The modified wound closure model starts with a rapid phase driven by the exponential term, reflecting the fast initial

healing after a wound is created. As time progresses, the influence of the exponential term diminishes, and the hyperbolic $a\sinh(t)$ becomes more prominent, indicating a slowing closure rate as the wound nears full closure. This combination of exponential decay and hyperbolic sine functions provides the model with the flexibility to accurately fit diverse wound closure data. Adjusting the parameters allows the model to capture the non-linear, time-dependent nature of the healing process. The equation was fitted to the experimental data using a MATLAB 2023 cftool inbuilt function.

To calculate cell migration velocity, time-lapse microscopy experiments were conducted using a CytoSMART Lux2 inverted microscope to track cell migration across the scratch in one field of view. Images were captured at 2 h intervals over 48 h, and velocity calculations were performed using a custom MATLAB code developed in-house (ESI Fig. 1†). Edge detection algorithms in MATLAB were used to generate contours and precisely trace the boundary between the migrating cells and the cell-free zone. Accurate identification of these edges was used to quantify cell migration velocity by tracking the movement of the cell fronts over time. An example scratch assay micrograph with a red contour trace to delineate the scratch cell edge margins is shown in ESI Fig. 2.† The central cleared area represents the wounded region within the confluent cell monolayer, with surrounding cells migrating into this space over time. The red lines superimposed on the image mark the detected edges of the migrating cells.

2.3.4. MTT assay to measure the effect of stressors in combination with GB-$Ti_3C_2T_x$ on HaCaT cell viability. Changes in keratocyte viability were measured using a Celltiter Non-radioactive Cell Proliferation MTT assay (Promega, UK). Mannitol solutions with osmolarities ranging from 300 to 800 mOsM were prepared using an initial 200 mg mL^{-1} stock solution, followed by a series of dilutions. Osmolarity was measured using a freezing point OSMOMAT 3000 osmometer. All solutions were sterilised by filtration through a 0.22 μm filter. HaCaT cells were then seeded at a density of 2×10^5 cells per mL into the wells of a 48-well plate and incubated at 37 °C, 5% CO_2 for 24 h. The medium was replaced with the prepared mannitol solutions, and cells were incubated for 24 h. 100 μL MTT reagent (5 mg mL^{-1}) was added to each well and incubated for 4 h, followed by removing and adding 100 μL DMSO. Absorbance was measured at 590 nm using an EL808 Microplate Reader (BioTek, USA). A 550 mOsM mannitol solution was selected to induce hyperosmotic stress in the scratch assays. On completion of the 48 h scratch assay, an MTT assay was again used to assess changes in cell viability on exposure of cells to each of the test conditions described in 2.3.2. 500 μL of MTT reagent was added to the wells of each plate. Cells were incubated at 37 °C, 5% CO_2 for 4 h, 500 μL DMSO was added, 100 μL of each condition was transferred to a 96-well plate, and absorbance was measured at 590 nm.

2.3.5. Live/dead staining to measure the effect of stressors in combination with GB-$Ti_3C_2T_x$ on HaCaT cell viability. HaCaT cells were seeded into the wells of 12 well, $Ti_3C_2T_x$ coated and uncoated plates at a seeding density of 1×10^5 cells per mL and incubated at 37 °C, 5% CO_2 for 24 h. Cells were then treated with either mannitol (550 mOsM) or GB (10 mM) for comparison against a cell-only negative control or a 4 mM hydrogen peroxide (H_2O_2) positive control. After a 24 h incubation period, the cells were stained with Live/Dead™ 2× stock containing calcein-AM and BOBO-3 iodide (Invitrogen, UK) and incubated for 15 min at room temperature. Cells were imaged using a Leica TCS SP5 confocal microscope (Leica Microsystems Ltd, UK) at excitation/emission wavelengths of 488/515 nm and 570/602 nm for calcein-AM and BBO-3 iodide, respectively.

2.3.6. Enzyme-linked immunosorbent assay (ELISA) to measure the effect of GB-$Ti_3C_2T_x$ on osmotic stress induced HaCaT secretion of inflammatory cytokines following scratch. The effect of $Ti_3C_2T_x$ and GB on inflammatory cytokine production by osmotically stressed keratocytes was compared to that of cell-only and bacterial LPS exposed cells using a human IL-6 BDOptEIA ELISA (BD Biosciences UK). 24 h after the cell scratch assay was initiated, 500 μl of the cell conditioned media was collected and analysed for the presence of IL-6. Samples were analysed neat, according to the manufacturer's protocol with the exception of mannitol, mannitol, and LPS, $Ti_3C_2T_x$ mannitol, and $Ti_3C_2T_x$ mannitol LPS which were diluted 2-fold.

2.3.7. qRT-PCR assay to measure the effect of GB-$Ti_3C_2T_x$ on osmotic stress induced upregulation of inflammatory cytokine and chemokine gene expression following scratch. Changes in marker inflammatory cytokine and chemokine gene expression profile on exposure to scratch test conditions described in 2.3.2 were measured using qRT-PCR. The scratch assay was set up as described in 2.3.2, and plates were incubated for 6 h, following the addition of LPS, mannitol, and GB to $Ti_3C_2T_x$ coated and uncoated plates. Cells were then trypsinised and centrifuged at 12*g* or 5 min (Thermofisher Scientific, Heraeus PICO 17 microcentrifuge) to collect cell pellets. RNA was extracted using the RNeasy® Mini Kit (Qiagen, UK) and quantified using a Nanodrop spectrophotometer (Thermofisher Scientific, NanoDrop One, UK). Genomic DNA was removed, and cDNA synthesis was performed using a QuantiTect® Reverse Transcription Kit (Qiagen, UK). Gene expression analysis of primers CXCL1, CXCL8, IL-1α, IL-1β, and IL-6 was carried out using the Rotor-Gene® SYBR® Green PCR Kit (Qiagen, UK), with GAPDH as the reference housekeeping gene.

2.3.8. Apoptosis assay to assess the effect of GB-$Ti_3C_2T_x$ on stressor induced HaCaT cell apoptosis. Potential keratocyte protection from osmotic stress-induced apoptosis using $Ti_3C_2T_x$ coatings was assessed by flow cytometry detection of annexin V expression. Cells were seeded in a 24-well plate at a concentration of 2×10^5 cells per mL, using both $Ti_3C_2T_x$ coated and uncoated conditions. Following incubation for 24 h at 37 °C in 5% CO_2, the cells were treated with the following conditions: untreated cell-only control, 4 mM H_2O_2 positive control, mannitol 550 mOsM, and mannitol 650 mOsM. After a 4 h incubation, the cells were trypsinised and washed 3 times with cold PBS at 12*g* or 5 min following the FITC

Annexin V Apoptosis Detection Kit I manufacturer's instructions (BD Biosciences, UK). The cells were then resuspended in binding buffer, stained with 2 μL of FITC conjugated Annexin V and 2 μL of Propidium Iodide (PI). Apoptosis status was measured using a Beckman Coulter CytoFLEX flow cytometer (Beckman Coulter Life Sciences, UK), recording a minimum of 10 000 events per sample at a medium flow rate. Cells were gated to exclude debris, and compensation settings were applied using the appropriate unstained and single-stained controls to account for spectral overlap between the FITC and PI stains. The inbuilt CytExpert software was used for data analysis.

2.3.9. Rhodamine phalloidin staining to assess the effect of GB-$Ti_3C_2T_x$ on osmotic stress induced changes in HaCaT cytoskeletal structure. Changes in actin cytoskeletal structure were visualised by confocal microscopy using rhodamine phalloidin. HaCaT cells were seeded at a density of 1×10^5 cells per well in a 12-well plate containing $Ti_3C_2T_x$ coated and uncoated wells. Following overnight incubation at 37 °C in 5% CO_2, test condition cells were treated with 550 mOsM mannitol and plates were incubated for a further 4 h. Cells were then washed in PBS, fixed with 3.7% formaldehyde for 10 min, permeabilised using 0.1% Triton-X for 10 min and incubated with rhodamine phalloidin (Thermofisher Scientific, UK) for 20 min and then after three PBS washes, cells were incubated with DAPI (Thermofisher Scientific, UK) for 20 min with another three PBS washes after. Samples were imaged using confocal microscopy at excitation/emission wavelengths of 540/565 nm for rhodamine phalloidin and 350/465 nm for DAPI.

2.4. Synthesis and testing of a $Ti_3C_2T_x$-*t*Bu-GB-microgel wound dressing

2.4.1. Synthesis and characterisation of betaine ester 'prodrug', *tert*-butyl glycine betainate (*t*Bu-GB). Sustained release of GB was accomplished through hydrolytic degradation of the *tert*-butyl alcohol ester of GB, which acted as a GB-releasing 'prodrug'. This ester was synthesised by the reaction of trimethylamine (TMA) (Fluorochem, UK) with *tert*-butyl bromoacetate (TBB) (Fisher Scientific, UK). 5 mL (25 mmol) TBB was added to 45 mL acetone at room temperature with stirring at 0 °C. This was followed by slowly adding 15 mL of TMA (2 M) in tetrahydrofuran (THF) with vigorous stirring for 5 min until the formation of a white precipitate. After 25 min of further stirring, the white precipitate was collected by filtration and recrystallised from isopropyl alcohol/acetone. 5.1 g (80% yield) of a white, crystalline product, 2-(*tert*-butoxy)-*N*,*N*,*N*-trimethyl-2-oxoethan-1-aminium bromide (*t*Bu-GB) was obtained. A reaction scheme is shown in ESI Fig. 3.† The structure of *t*Bu-GB was confirmed using mass spectrometry and Fourier transform infrared spectrometry (FTIR) (Bruker HCT Ultra mass spectrometer, Bruker, USA; PerkinElmer Spectrum Two FTIR spectrometer, PerkinElmer, UK).

2.4.2. Synthesis and loading of polyacrylate based microgels with *t*Bu-GB. Acrylic acid (AA) (Sigma Aldrich, UK) and ethylene glycol dimethacrylate (EGDMA) (Sigma Aldrich, UK) were mixed in a 2 : 1 weight ratio. 1.5 mL of this monomer mixture was added dropwise to 20 mL of a vigorously stirred deionised (DI) water solution containing the initiator, ammonium persulfate (2.0% w/v). 150 μL of tetramethylethylenediamine (TEMED) (Fisher Scientific, UK) were then added to the resulting coarse emulsion to catalyse the generation of radical species from APS, enabling the polymerisation of AA and EGDMA to progress at room temperature. After mixing for 15 min under high shear, poly(acrylic acid-*co*-EGDMA) was isolated by filtration, washed three times each with acetone, DI water, and methanol and dried.

The acrylate-based microgels were then loaded with *t*Bu-GB by a simple soak-swell-rinse-dry method designed to saturate the gel with *t*Bu-GB through electrostatic interaction. Briefly, 0.2 g of the dry gel was stirred in 2.5 mL DI water containing 0.5 g *t*Bu-GB for 5 min to initiate electrostatic pairing of negatively charged acrylate and positively charged betaine ester, *i.e.* $[t\text{Bu-GB}]^+/[\text{PAA-}co\text{-EGDMA}]^-$. Excess water and unbound solutes were removed by filtration, and the solids were allowed to air dry. The loading procedure was repeated three times to saturate the gels with *t*Bu-GB. Approximately 10 mg of plain polyacrylate microgels and *t*Bu-GB loaded polyacrylate microgels were dispersed in 1 mL DI water and were analysed for changes in size and polydispersity using Dynamic Light Scattering (DLS) (Mastersizer 3000, Malvern, UK). A suspension prepared in the same way was imaged using light microscopy. *t*Bu-GB loading into the polyacrylate based microgels was confirmed by FTIR.

2.4.3. Elution of GB from *t*Bu-GB loaded polyacrylate microgels. Isolated $[t\text{Bu-GB}]^+/[\text{PAA-}co\text{-EGDMA}]^-$ microgels were suspended in PBS at 80 mg in 500 μL PBS. At regular intervals (0, 1.5, 3, 6, 24, 48 h), the supernatant was collected by filtration and the solids were resuspended in 500 μL fresh PBS for further timed incubation. Analysis of the supernatant for its GB content was carried out by liquid chromatography–mass spectrometry (LC-MS). The accumulated GB concentration from each sample was used to construct a release profile for increasing [GB] over time.

LC-MS analysis was conducted using a Burker HCT Ultra Electrospray ionisation/ion trap mass spectrometer (Bruker, USA) interfaced with an Agilent 1200 series higher performance liquid chromatograph (HPLC) (Agilent Technologies, USA). The stationary phase was a Kinetex silica 100 × 3.0 mm hydrophilic interaction chromatography (HILIC) column (Phenomenex, USA). An isocratic elution was performed with a mobile phase comprising 65% v/v acetonitrile, 17% v/v water, 17% v/v methanol, 1% v/v acetic acid, and 3.9 mg mL^{-1} ammonium acetate. All LC-MS solvents and additives were purchased from Fisher Scientific, UK. Extracted ion count (EIC) chromatograms were used for data analysis; the target ion, 140 *m*/*z*, was the most abundant for GB (corresponding to the sodium adduct of GB: $[^{117}\text{GB}\cdot^{23}\text{Na}^+]$). The molecular ion corresponding to *t*Bu-GB, 174 *m*/*z*, was used to generate the EIC chromatograms for *t*Bu-GB.

2.4.4. Fabrication of a $Ti_3C_2T_x$-*t*Bu-GB microgel wound dressing and assessment of cytotoxicity. Polyacrylate microgels were synthesised and loaded with GB as described in section 2.4.2. 45 mg of GB saturated microgel was then resuspended

in 500 μL of acetone, pipetted onto 1 cm^2 discs of a cellulose based commercial wound dressing disc (Kerracel™, 3 M) and allowed to air dry overnight. Separate 1 cm^2 dressing discs were spray-coated with 5 mg mL^{-1} $Ti_3C_2T_x$ and adhered to the microgel impregnated dressing component using a thin layer of cyanoacrylate glue around the edge of the dressing.

The *t*Bu-GB microgels and $Ti_3C_2T_x$-*t*Bu-GB microgel dressings were UV-sterilised. Samples were incubated at 37 °C for 28 h on an orbital shaker (SI50 Orbital Incubator Platform Shaker, Stuart Scientific) in 1 mL media, adjusted to 300, 550 or 650 mOsM, prior to collection of the conditioned media. HaCaT cells were seeded at 5×10^4 cells per well in a 48-well plate and incubated at 37 °C in 5% CO_2 for 24 h. 500 μL of the conditioned media for each sample type (cell only, *t*Bu-GB microgel, $Ti_3C_2T_x$-*t*Bu-GB microgel dressing) was then transferred to the relevant well and plates were incubated for 24 h at 37 °C in 5% CO_2. The MTS assay was then carried out as described in 2.3.4.

2.4.5. GB Elution over time from a $Ti_3C_2T_x$-*t*Bu-GB microgel wound dressing. $Ti_3C_2T_x$-*t*Bu-GB microgel dressings prepared as described in section 2.4.4 were submerged in 1 mL PBS at 37 °C. At regular timepoints of 0, 2, 4, 6, 8, 24, 48 h, the supernatant was removed for analysis by LC-MS and replaced with a further 1 mL of PBS. LC-MS analysis was carried out as described in 2.4.3. Accumulated values for GB were used to construct a release profile for *t*Bu-GB and GB from the dressings over time.

2.5. Statistical analysis

Data was analysed using GraphPad Prism version 8.0.1 (GraphPad Software, San Diego, CA). Significance was determined using a two-way analysis of variance (ANOVA) and a Tukey's multiple comparison *post hoc* test with a significance value set at $p < 0.05$. All data was expressed as mean ± standard error of the mean (SEM) for 3 experimental repeats unless otherwise stated. First-order curve fitting was performed in MATLAB 2021 using the Curve Fitting Tool, allowing visualization of 95% confidence bounds and extraction of key metrics such as coefficient values, R^2 and RMSE.

3. Results and discussion

3.1. Characterisation of $Ti_3C_2T_x$ and $Ti_3C_2T_x$ coatings

UV-Vis spectroscopy was used to measure the absorbance of dilute colloidal $Ti_3C_2T_x$ solutions, as shown in Fig. 1(a). A broad peak was detected in the 700–800 nm range with a peak maximum at 766 nm. Following Beer-Lambert's law, a calibration curve was constructed (ESI Fig. 4†), leading to the calculation of an extinction coefficient of 29.78 mL mg^{-1} cm^{-1}, comparable to values reported in the literature.[28] DLS was used to estimate the average hydrodynamic size distribution of the $Ti_3C_2T_x$ colloidal solutions (Fig. 1(b)). Two peaks were identified: a major peak, which accounted for >97% of the distribution, with an average size of 260.6 nm, and a minor peak representing 3% of the distribution, estimated to be 51.3 nm, with an average polydispersity index of 0.22. The XRD pattern of Ti_3AlC_2 exhibited sharp, well-defined peaks (Fig. 1(c)). In contrast, on etching away the Al layer to form $Ti_3C_2T_x$, the XRD pattern showed a significant shift of the (002) peak due to increased interlayer spacing, as well as a disappearance of the higher ordered peaks. These changes demonstrate the successful topochemical transformation from bulk Ti_3AlC_2, MAX phase, to the 2D $Ti_3C_2T_x$ flakes.[46] The SEM images of the $Ti_3C_2T_x$ spray-coated well plate indicated a 1–2 μm thick uniformly distributed surface layer (ESI Fig. 4†).

The hydrophilicity of $Ti_3C_2T_x$ as a coating, when spray-coated onto a solid support, was investigated using contact angle analysis (Fig. 1(d and e)). The presence of the coating significantly reduced the contact angle from 58.20° ± 2.46 to 22.47° ± 2.40, indicating enhanced wettability and suitability for a smart wound dressing application. Hydrophilic materials enhance the ability of dressings to absorb and retain moisture and solutes away from the wound bed, including inflammogenic proteins, which may delay the wound healing process,[26] facilitating the efficient loading and sustained release of hydrophilic drugs.[27] Hydrophobic coatings, on the other hand, are less suitable for wound dressing applications as, for example, they reduce the ability of the substrate material to absorb wound exudate.

3.2. Assessing the osmoprotective effects of GB-$Ti_3C_2T_x$ using an *in vitro* HaCaT model of wound repair

3.2.1. $Ti_3C_2T_x$ coatings and GB synergistically improve scratch wound closure and protect against osmotic stress induced repression of HaCaT cell migration. The effect of mannitol-induced osmotic stress on scratch wound closure and the protective effects of $Ti_3C_2T_x$ and 10 mM GB on keratocyte ability to migrate and close the wound are shown in Fig. 2(a). The GB concentration was selected based on the concentration range used in previous studies.[38,39,47] The results compare normal, iso-osmotic conditions (300 mOsM) and mannitol-induced hyperosmotic stress conditions (550 mOsM). The percentage of wound closure for each condition was normalised, with '1' representing complete wound closure. The fitted curves, represented by solid lines and with a 95% confidence level, demonstrated agreement between the data and the proposed mathematical models. R^2 values were greater than 0.99 for each curve fit (ESI Table 1†). Mannitol-induced hyperosmotic stress significantly reduced the rate of migration when compared to the iso-osmotic control condition, and keratocytes were unable to close the scratch. After 48 h under mannitol-induced hyperosmotic stress, normalised wound closure values reach only 0.64 compared to complete closure of the scratch under iso-osmotic cell-only conditions. However, when the scratch assay was conducted under hyperosmotic conditions in the presence of $Ti_3C_2T_x$, the wound closure rate improved almost to the level of the iso-osmotic control. Normalised wound closure reached 0.99 within 48 h and more rapidly than other hyperosmolar conditions. Treatment with the osmoprotectant, GB, in the absence of $Ti_3C_2T_x$ also improved the cell response to osmotic stress com-

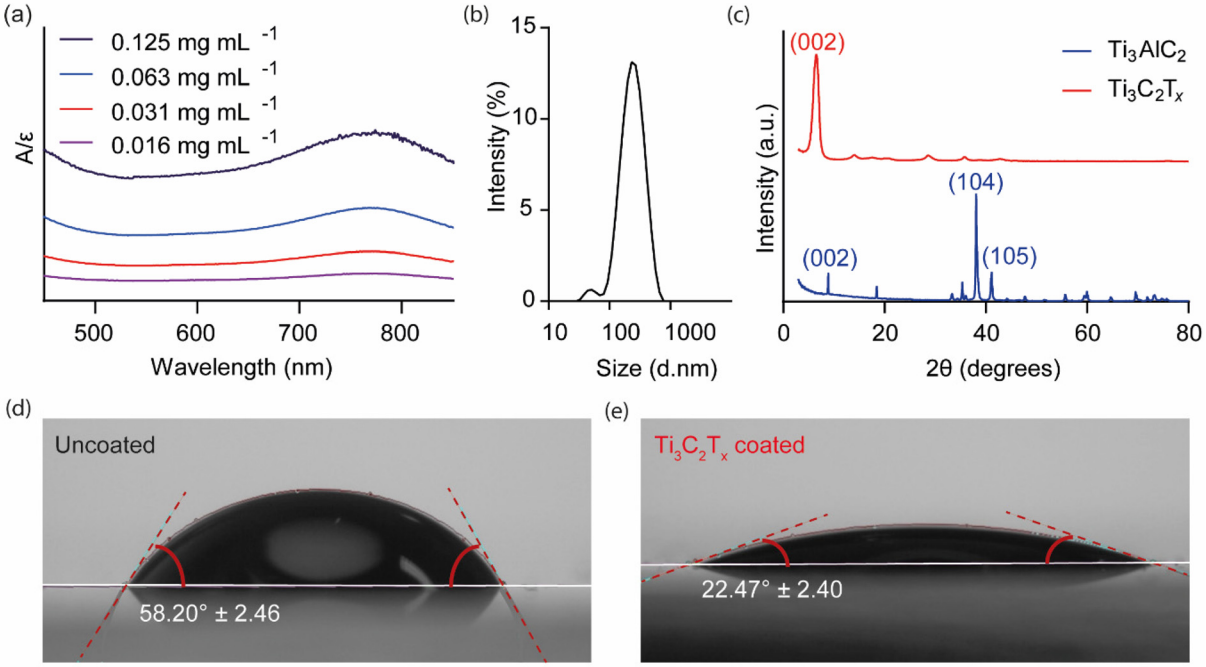

Fig. 1 Physical characterisation of $Ti_3C_2T_x$. (a) UV-Vis spectroscopy of $Ti_3C_2T_x$ solutions of varying concentrations normalised to the molar extinction coefficient (ε = 29.78 L g^{-1} cm^{-1}) calculated from the calibration curve (ESI Fig. 5†). (b) Dynamic light scattering was used to determine the particle size and distribution of the $Ti_3C_2T_x$ solution. (c) X-ray diffraction comparing the crystal structure of Ti_3AlC_2 to the synthesised and vacuum-filtered $Ti_3C_2T_x$ film (Cu K_α radiation source (λ = 1.5406 Å) at 40 kV and 15 nA beam current). (d) The contact angle of the uncoated (58.20 ± 2.46°) and (e) $Ti_3C_2T_x$ coated (22.47 ± 2.40°) glass slide surface.

pared to the mannitol-treated condition, with wound closure reaching 0.81 after 48 h. In the group treated with both GB and $Ti_3C_2T_x$, the impact of GB was augmented. GB treatment improved scratch closure over time, and its combination with $Ti_3C_2T_x$ further amplified this effect.

The rate coefficient data also confirms the positive impact of $Ti_3C_2T_x$ on wound closure (ESI Tables 2 and 3†). Coefficient *b* values, representing the initial migration rate, were consistently higher for the $Ti_3C_2T_x$ groups compared to the cell-only, cells with mannitol, and cells with mannitol plus GB groups. Coefficient c values, modulating the impact of the hyperbolic sine term in the model and representing the later stages of wound closure, were lower for the $Ti_3C_2T_x$ group compared to the mannitol and mannitol GB group in late-phase keratocyte closure of the wound. The lower value of coefficient c reflects a slower transition in the middle phase but enables rapid closure at later time points due to less influence from the hyperbolic term. It may be that $Ti_3C_2T_x$ is less influential in the mid to late stages of migration. Alternatively, the removal of $Ti_3C_2T_x$ between the cell margins on the application of the scratch may reduce the impact of $Ti_3C_2T_x$ in mid to late-phase migration.

The positive impact of $Ti_3C_2T_x$ and GB of keratocyte migration was confirmed by the keratocyte velocity data. Time-lapse microscopy imaging and a custom MATLAB code were used to determine the velocity of the wound edge keratocytes as they migrated to close the scratch (ESI Fig. 2†). Fig. 2(b) and (c) show the mean migration velocity (MV) of cells over time without and with a $Ti_3C_2T_x$ coating, respectively, and indicate a significant reduction in initial keratocyte MV under mannitol-induced osmotic stress conditions, an increase in keratocyte MV for keratocytes in contact with $Ti_3C_2T_x$ coatings under iso-osmotic and hyperosmotic conditions. They also show a further increase in keratocyte MV in combined GB and $Ti_3C_2T_x$ coated conditions. Under iso-osmotic cell-only conditions, keratocyte MV remained relatively high (~0.018 μm s^{-1}) until wound closure by 24 h. Iso-osmotic $Ti_3C_2T_x$ coated keratocyte MV was initially rapid (~0.022 μm s^{-1}), declining at 8 h until wound closure by 24 h. For mannitol-treated, osmotically stressed cells initial MV was much slower (~0.014 μm s^{-1}), with no improvement or closure of the scratch wound by 48 h. In contrast, keratocytes cultured on $Ti_3C_2T_x$ coatings under mannitol conditions showed a rapid MV (~0.018 μm s^{-1}), which slowed at 8 h to close the wound by 36 h. GB mannitol also induced an initial rapid MV (~0.017 μm s^{-1}) with a gradual decline to close the wound at 48 h. GB mannitol in the presence of a $Ti_3C_2T_x$ coating induced an initial rapid MV (~0.021 μm s^{-1}) to close the wound by 36 h and more rapidly than in the GB mannitol alone, indicating the protective effect of $Ti_3C_2T_x$ and GB combined (ESI Table 4†).

Whilst normal wound repair relies on a more complex series of signalling cues involving multiple cell types, *in vitro* modelling using a single cell type scratch assay allowed the impact of individual variables on keratocyte behaviour to be more easily defined. Mechanisms by which these variables affect scratch closure can then be considered in more detail. Under normal conditions epidermal keratocyte wound repair

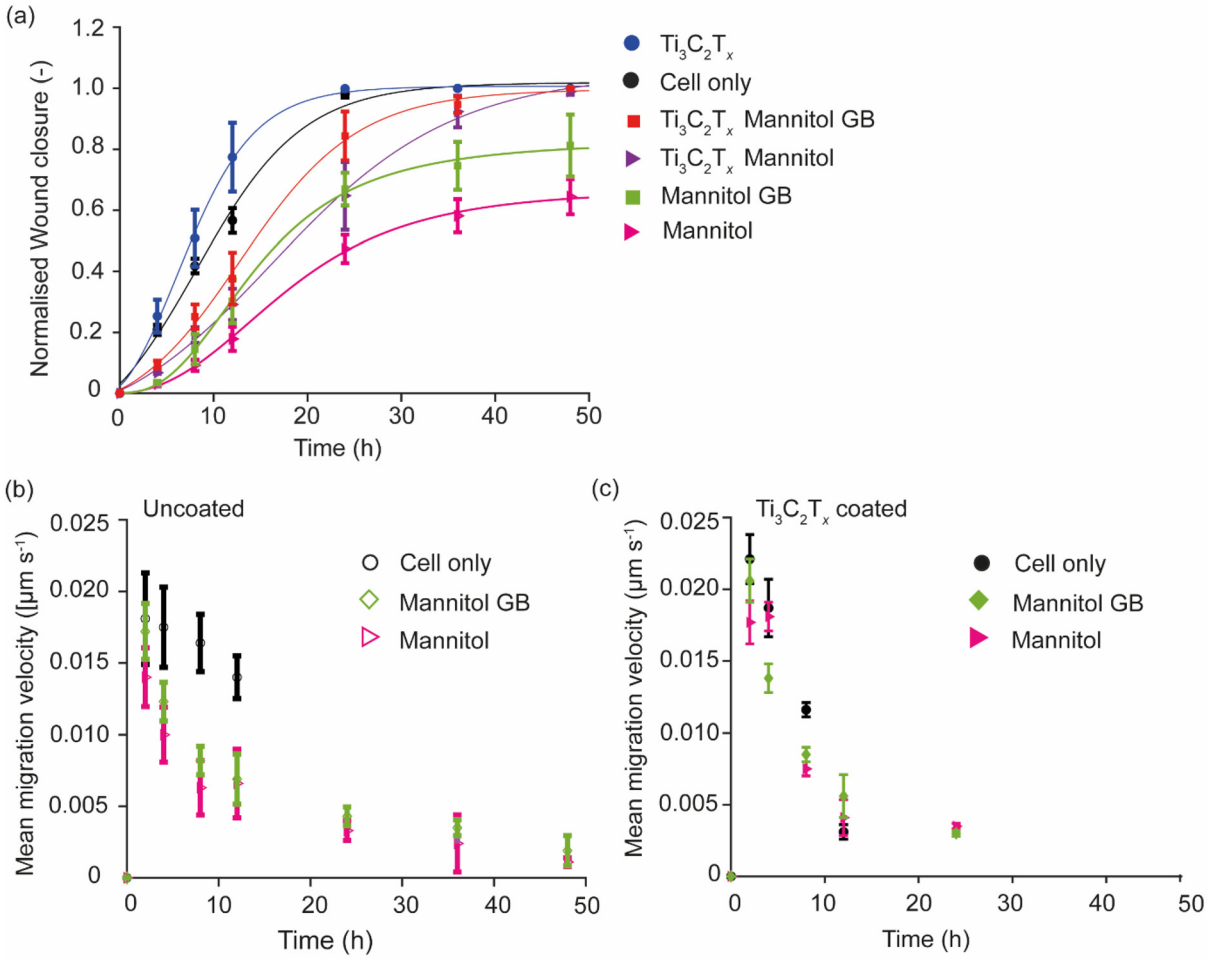

Fig. 2 Cell migration scratch assay results indicating a significant reduction in keratocyte migratory capacity under mannitol-induced, hyperosmotic stress conditions and a significant protective effect for cells grown on $Ti_3C_2T_x$ coatings to more rapidly close the scratch, (a) normalised wound closure (WC) over time, comparing keratocyte scratch closure under iso-osmotic conditions to scratch closure under hyperosmolar conditions in the presence and absence of $Ti_3C_2T_x$ coatings and GB. Across all cases, the curve fit yielded an R^2 value >0.99. (b) Mean migration velocity (MV) of cells over time under normal iso-osmolarity (cell-only), mannitol-induced hyperosmolarity (mannitol), and mannitol-induced hyperosmolarity with GB (mannitol GB) in uncoated and (c) $Ti_3C_2T_x$ coated conditions, (n = 3, mean ± SD).

is typically dependent on the inherent regenerative abilities of both a proliferative keratocyte fraction and the cut edge keratocytes. These cells respond to signalling cues and change their cytoskeletal network to migrate across a scratch and gradually close the wound.[48] Hyperosmotic stress provokes an altered cell repair response, including cell shrinkage, protein and DNA damage, and changes to cytoskeletal structure, all of which will limit migratory capacity. $Ti_3C_2T_x$ has a unique combination of properties to mitigate the upregulation of damage-associated pathways in keratocytes. These include high electrical conductivity, small solute intercalation properties, hydrophilicity, and a reactive surface chemistry, all of which are likely to contribute to a favourable environment for cellular activities necessary for wound healing. For example, $Ti_3C_2T_x$ may augment the impact of intracellular transient electrical behaviour arising from changes in molecular machinery, such as microfibrillar rearrangement to more rapidly mediate cell migration and wound closure. The presence of a naturally occurring, water-soluble, osmo-adaptive mediator, such as GB, may also benefit the disrupted wound bed environment. GB resists the effects of osmotic stress by stabilising cell volume, protein structure, enzyme activity, inflammatory upregulation, and other damaging effects of osmotic shock. Pre-incubation of keratocytes with GB stabilised the intracellular environment, allowing retention of migratory response and scratch repair despite external hyperosmotic stress conditions. Given the combined, synergistic effects of $Ti_3C_2T_x$ and GB on improved wound closure rate, subsequent experiments sought to determine the mechanisms by which they may act for therapeutic benefit to reverse the negative impact of osmotic stress on aspects of the keratocyte wound repair response.

3.2.2. $Ti_3C_2T_x$ coatings and GB are non-toxic to HaCaT cells under conditions of osmotic stress. Viability assays were used to determine whether cell death on exposure to $Ti_3C_2T_x$/GB conditions or osmotically-induced cytotoxicity contributed to the observed changes in wound healing response after

exposure to osmotic stress. The MTT cell viability data are shown in Fig. 3(a) and compared the following conditions: untreated, $Ti_3C_2T_x$ treated HaCaT cells to mannitol (550 mOsM) treated, GB (10 mM) and LPS (5 μg mL^{-1}). No significant reduction in cell viability was observed under all conditions, indicating that cell death did not contribute to the differences observed in migration rate in the wound closure model ($p > 0.05$). This observation was further supported by live/dead staining to indicate the presence of viable, green fluorescent or red fluorescent dead cells (Fig. 3(b)). Viable cells were maintained in all conditions in comparison to the cytotoxic H_2O_2 (4 mM) control, in which all cells exhibited red fluorescence confirming cell death.

3.2.3. $Ti_3C_2T_x$ coatings and GB significantly repress osmotic stress induced upregulation of cytokine and chemokine inflammatory markers. Given the role of osmotic stress on inflammation in non-healing wounds and the suspected synergistic anti-inflammatory effects of GB and $Ti_3C_2T_x$, upregulation of key inflammatory pathways under scratch assay conditions was measured using qPCR and ELISA. Fig. 4 compares changes in inflammatory cytokine IL-6 protein and IL-6 mRNA (Fig. 4(a and b)), IL-1α, IL-1β, CXCL1, CXCL8 mRNA expression (Fig. 4(c–f)). A significant increase in all inflammatory markers was observed 24 h after scratch assay initiation under mannitol-induced hyperosmotic stress conditions compared to the iso-osmotic cell-only control ($p < 0.0001$). This effect was potentiated by the presence of bacterial LPS, suggesting that in the presence of this bacterial endotoxin, the hyperosmotic stress inflammatory response is more severe. In all cases, $Ti_3C_2T_x$ significantly reduced the upregulation of these markers, supporting previous literature in other cell models and further evidencing a role for this material in the repression of hyper-inflammatory response.[26,49] GB also significantly reduced the upregulation of these markers in all cases, in the presence and absence of $Ti_3C_2T_x$ but more so in combination with $Ti_3C_2T_x$ coatings. In both the ELISA and qPCR, LPS treatment (used to simulate an infection-like inflammatory response), did not result in any significant changes in gene expression compared to the control group for all primers. However, when LPS was combined with mannitol, a significant increase in proinflammatory gene expression was observed compared to the mannitol condition alone. This suggests that the combination of LPS and osmotic stress amplifies the inflammatory response, suggesting that LPS-spiked infection primes osmotic stress-induced inflammation.

The results of the qPCR and ELISA support the results of the keratocyte scratch closure assay, demonstrating that both $Ti_3C_2T_x$ and GB are potent anti-inflammatory agents, but moreover, that the combination of the two exerts a synergistic effect which has a greater effect than either treatment alone. Indeed, it is well-known that GB stabilises cell volume and protein structure in plant, animal, and bacterial cells exposed to osmotic, cryogenic, or desiccant stress,[50–55] and that its presence has striking effects on the downregulation of proinflammatory cytokines in, for example, osmotically stressed ocular and hepatic cells.[34,38,56–58] $Ti_3C_2T_x$, while emerging only relatively recently compared to GB, is known to possess potent anti-inflammatory properties, with studies reporting its ability to reduce proinflammatory cytokine expression in LPS-stressed

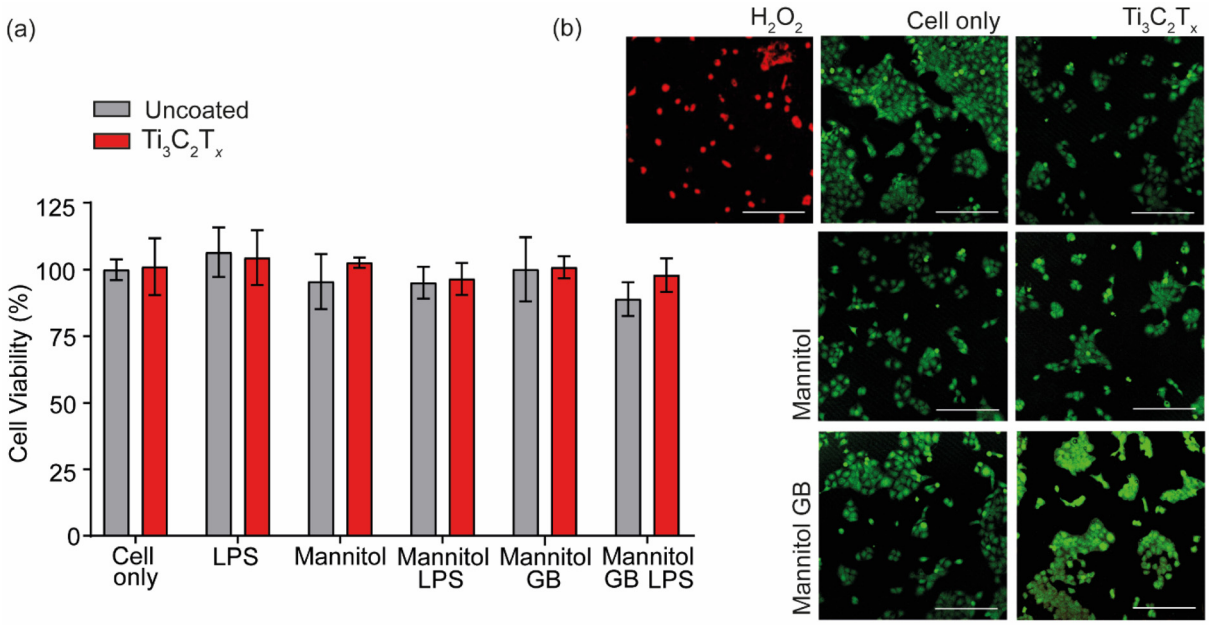

Fig. 3 (a) Cell viability assay indicating no significant cytotoxic effects on keratocytes exposed to all conditions (cell-only, LPS, mannitol (550 mOsM), mannitol and LPS, mannitol and GB (10 mM), mannitol, GB and LPS) in the presence and absence of $Ti_3C_2T_x$ coatings ($n = 3$, mean ± SEM, $p < 0.05$, scale = 250 μm). (b) representative confocal images of live/dead stained keratocytes 24 h after treatment with each condition in comparison to a cytotoxic H_2O_2 (4 mM) control.

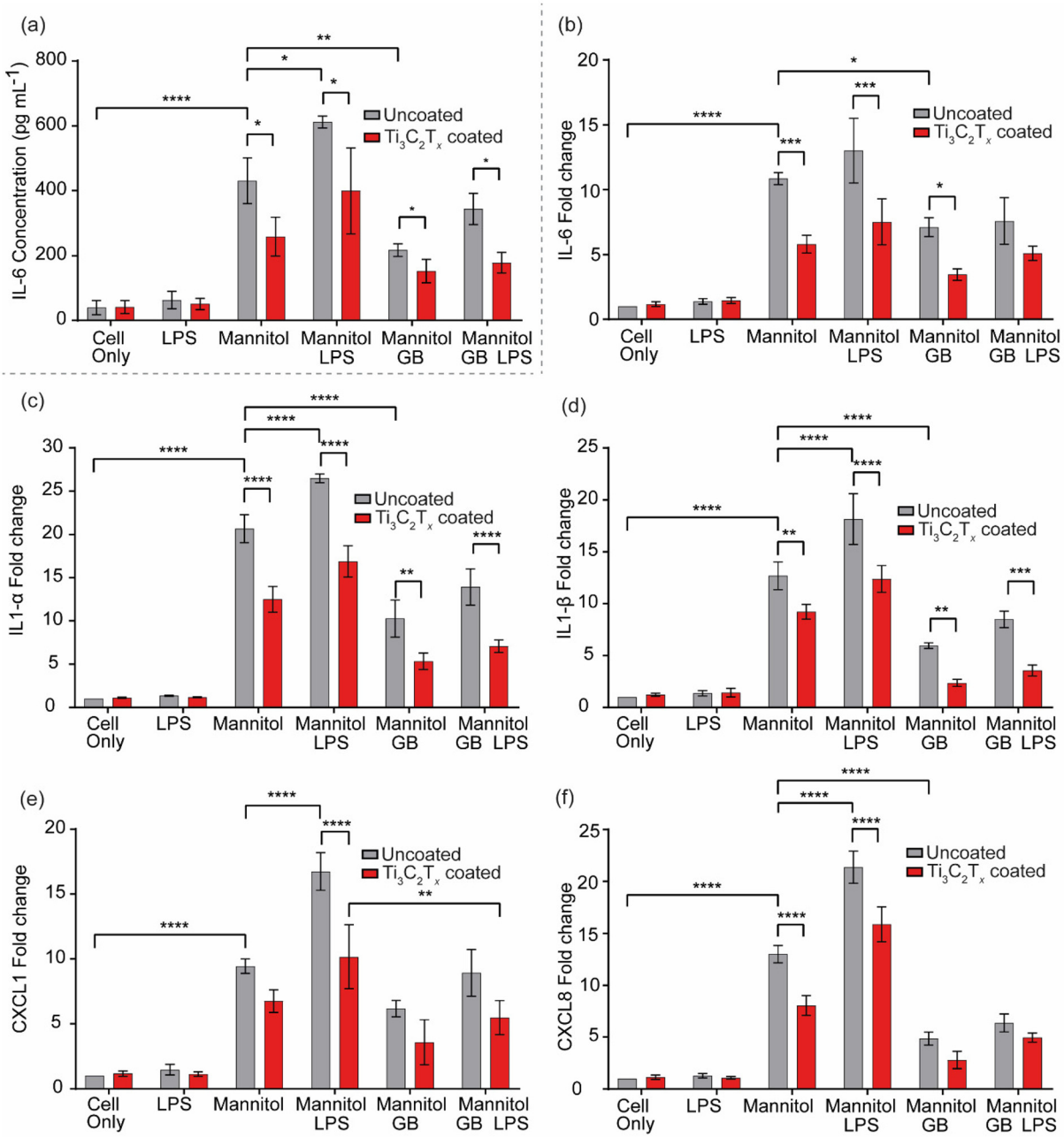

Fig. 4 Repression of HaCaT keratocyte inflammatory response to osmotic stress following $Ti_3C_2T_x$ GB treatment. (a) ELISA IL-6 production of keratocytes treated with $Ti_3C_2T_x$, LPS, mannitol (550 mOsM), GB (10 mM). (b) qRT-PCR IL-6 production of keratocytes exposed to the same treatments detailed above. (c) qRT-PCR IL-1α. (d) qRT-PCR IL-1β. (e) qRT-PCR CXCL1. (f) qRT-PCR CXCL8. Significance was determined using a two-way ANOVA and *post-hoc* Tukey's multiple comparison test (*p < 0.05, **p < 0.01, ***p < 0.001, ****p < 0.0001) (mean ± SEM, n = 3).

cells.[25,26] $Ti_3C_2T_x$ is also known to have antioxidant properties that could reduce oxidative stress at the wound site,[59] providing an environment that is more conducive to rapid healing.

3.2.4. $Ti_3C_2T_x$ coatings protect against osmotic and H_2O_2 stress induced HaCaT cell apoptosis. To investigate the role of apoptosis in keratocyte response to hyperosmotic and H_2O_2 induced stress and the potential protective effects of $Ti_3C_2T_x$, an apoptosis study was carried out using flow cytometry (Fig. 5). Mannitol treatments at 550 and 650 mOsM were compared because the MTT data showed no significant impact on cell viability at the 550 mOsM condition. In support of the viability data, the majority of cells remained viable in all of the 550 mOsM conditions (Fig. 5a and b). No significant increase in apoptosis status was observed for the 550 mOsM mannitol-induced hyperosmotic stress compared to the cell-only condition. In contrast, the 650 mOsM hyperosmotic condition showed a significant increase in the fraction of apoptotic cells (p < 0.0001). Incubation of keratocytes under the same con-

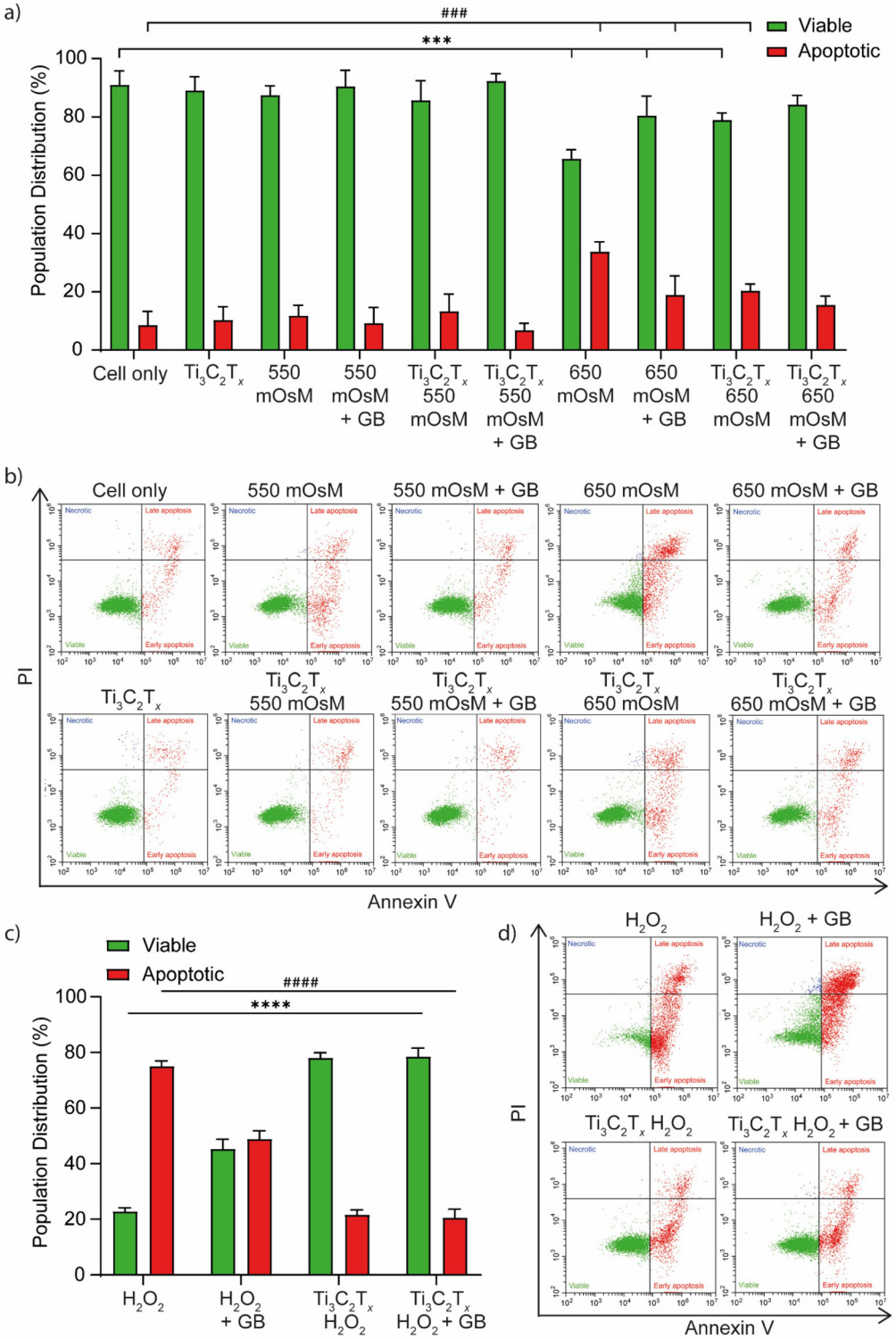

Fig. 5 $Ti_3C_2T_x$ coatings protect against osmotic and H_2O_2 stress induced HaCaT cell apoptosis. (a) Flow cytometry data indicating viable and apoptotic cell fraction under conditions of iso-osmotic cell only and cell-$Ti_3C_2T_x$ controls, 550 mOsM cell only, GB, $Ti_3C_2T_x$ and GB-$Ti_3C_2T_x$ conditions, 650 mOsM cell only, GB, $Ti_3C_2T_x$ and GB-$Ti_3C_2T_x$ conditions with viable cell fractions shown in green and combined early and late-stage apoptotic cell fractions shown in red. (b) Representative dot plots of the flow cytometry data shown in a. (c) Flow cytometry data demonstrating oxidative stress induced apoptosis using 4 mM H_2O_2 and the protective effect of $Ti_3C_2T_x$, comparing conditions of cells with H_2O_2 GB, H_2O_2 $Ti_3C_2T_x$ and H_2O_2 GB-$Ti_3C_2T_x$ to an H_2O_2 cell only control. (d) Representative dot plots of the flow cytometry data shown in c. Significance was determined using a two-way ANOVA and *post-hoc* Tukey's multiple comparison test (Viable cell fraction, ***$p < 0.001$, ****$p < 0.0001$) (Apoptotic cell fraction, $^{\#\#\#}p < 0.001$, $^{\#\#\#\#}p < 0.0001$) (mean ± SEM; $n = 3$).

ditions in the presence of a GB-$Ti_3C_2T_x$ coating combination, reduced the apoptotic cell fraction to that of the iso-osmotic control, indicating a protective effect of the coating. On addition of an H_2O_2 (4 mM) apoptotic stressor a highly significant increase in apoptosis occurred ($p < 0.0001$) (Fig. 5c and d). However, in the presence of $Ti_3C_2T_x$ the apoptotic cell fraction was again reduced to that of the cell only control. This was not seen in the GB only condition indicating that $Ti_3C_2T_x$ alone protected the HaCaTs against oxidative stress induced apoptosis. The results demonstrate the ability of $Ti_3C_2T_x$ to rescue HaCaT keratocytes from apoptosis under hyperosmotic stress conditions of 650 mOsM and in the presence of an oxidative stressor, H_2O_2. This aligns with reports in the literature, where the material has been shown to scavenge various reactive oxygen and nitrogen species.[60,61]

3.2.5. $Ti_3C_2T_x$ coatings and GB protect HaCaT cells against osmotic stress induced alterations in HaCaT cytoskeletal structure. Identifying changes in intracellular actin filament (F-actin) distribution is a convenient marker of cytoskeletal rearrangement following exposure to a range of stressors in addition to altered cell morphology in the early stages of cell migration *in vitro*. Phalloidin staining, specifically binding to F-actin, showed differences in cell morphology and actin cytoskeletal structure in 550 mOsM mannitol-treated osmotically stressed cells. Keratocytes exposed to mannitol-induced hyperosmotic stress displayed a size reduction, indicating cellular shrinkage due to the osmotic gradient between the intracellular and extracellular compartments. This can be seen in the compact cell morphology and nuclear clustering of the keratocytes in Fig. 6 compared to the iso-osmotic control. In contrast, cells in the presence of GB and $Ti_3C_2T_x$ coating, exposed to mannitol, maintained a similar morphology to that of the untreated cells, with no signs of shrinkage. Results indicate a protective effect of both $Ti_3C_2T_x$ and GB alone and in combination against hyper-osmotic stress induced changes in cytoskeletal structure and cell shrinkage.

3.2.6. $Ti_3C_2T_x$-*t*Bu-GB-microgel wound dressings are biocompatible and induce slow elution of GB over time. Due to continual fluid replenishment within the wound bed, administration of a single dose of GB on the application of a wound dressing is unlikely to sustain a therapeutic concentration of GB in the wound bed throughout the timeframe required for an osmotically challenged wound to heal. However, extending the release lifetime of GB from drug reservoirs or biomedical implants such as hydrogels or microcapsules is difficult due to the small, hydrophilic nature of GB. These features commonly result in GB rapidly partitioning into aqueous surroundings, typically within the scale of minutes rather than hours or days, even with attempts to block diffusion through the use of, for example, high concentrations of hydrophobic barrier molecules.[39]

It was hypothesised that forming a cationic ester of GB with a short-chain alcohol and embedding this within a negatively charged reservoir/platform material for incorporation with $Ti_3C_2T_x$ into a wound dressing would enhance the former's release lifetime through a combination of two main mechanisms. Firstly, GB release from the ester would be controlled by a relatively slow chemical reaction (hydrolysis) rather than solely by (relatively rapid) diffusion. Secondly, the intact, cationic ester could be retained by electrostatic interaction at anionic pendant groups in a reservoir/platform material with an overall negative charge. A GB-releasing system was therefore designed based on *t*Bu-GB for use in combination with a negatively charged acrylic acid-based microgel, as shown in Fig. 7(a).

A successful synthesis of *t*Bu-GB was confirmed by mass spectrometry (ESI Fig. 6†) and FTIR (ESI Fig. 7†). Hydrolytic conversion of *t*Bu-GB into GB was confirmed by repeated sampling and LC-MS analysis of the same 2.5 mg mL^{-1} solution of *t*Bu-GB, in PBS, at 32 °C and pH 7.2 over 5 days. After 5 days, the LC-MS peak corresponding to *t*Bu-GB was not evident, while that corresponding to GB dominated the spectrum, confirming the conversion of *t*Bu-GB to GB in aqueous surroundings. The release profile of GB from *t*Bu-GB in this solution is shown in Fig. 7(b) and is approximately linear over the initial 24 h (during which 70% of the total measured GB is evolved), before entering a lag phase between 30 h and 120 h. A total of 330 μg mL^{-1} GB was released after 5 days. This is *ca.* 85% of the total releasable GB, recovered after degradation of a separate aliquot of the same 2.5 mg mL^{-1} stock, which was degraded into Na·GB and *tert*-butyl alcohol by exposure to highly alkaline conditions after spiking with 0.25 M NaOH. The release curve was fitted to a first order kinetic plot with curve in the form $M(1 - e^{(-x/T)})$. Here, M = 340.3 ± 49.7 M μg mL^{-1} represents the asymptotic maximum concentration of GB released, and T = 1.01 ± 0.36 is the time constant representing the rate at which the release approaches saturation.

An AA/EGDMA-based microgel was selected as the base material for the entrapment of the positively charged *t*Bu-GB. Polymerisation of the AA/EGDMA monomer combination is known to produce highly water-swellable, porous, and strongly negatively charged structures which can retain small, positively charged molecules, and even larger molecules such as proteins.[62] The polymerisation method was based on the works of Tuncel *et al.*, who studied the development of non-swellable and swellable AA/EGDMA microspheres by altering synthetic parameters,[63] and Hoare *et al.*, whose study detailed the impact of ionisable group distribution in microgels in the delivery of ionic drugs.[64] Due to the small molecular cross-section of *t*Bu-GB, a lower degree of swelling is more desirable in this case, as it can be expected to impact rate of elution *via* diffusion inhibition;[65] hence, a high cross-linker ratio of 2 : 1 AA : EGDMA was selected. Nonetheless, the retention and elution of the GB precursor, *t*Bu-GB, is expected to be primarily driven by the electrostatic interaction between negatively charged COO^- and positively charged $-N^+Me_3$ groups in the respective materials.

The prepared $[t\text{Bu-GB}]^+/[\text{PAA-}co\text{-EGDMA}]^-$ microgels presented as a fine powder once dried, with an average particulate size of 11.9 μm and an asymmetrical, aspherical morphology, forming aggregates and sediments readily in unstirred solu-

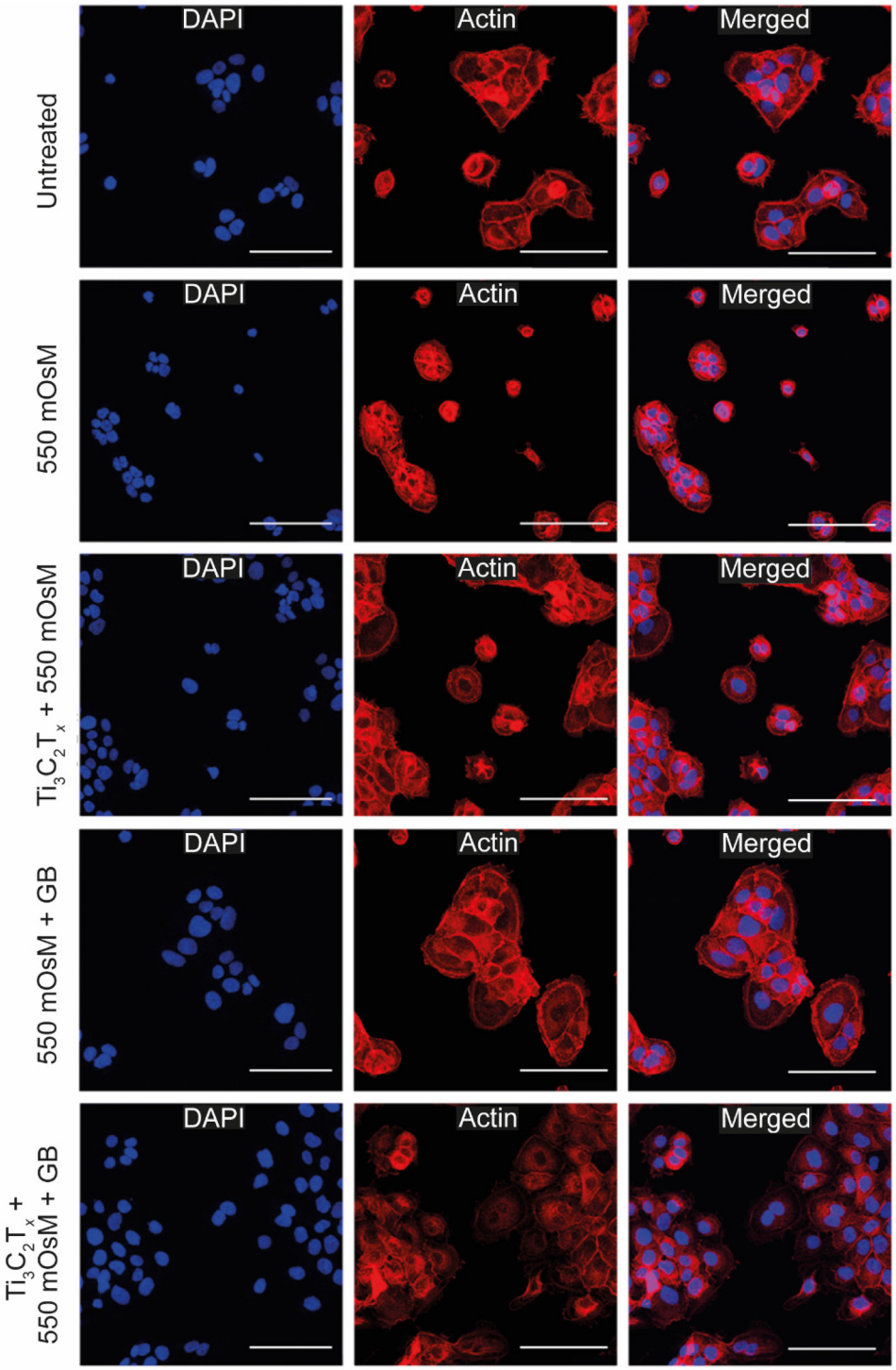

Fig. 6 Confocal micrographs showing actin cytoskeletal structure of HaCaT keratocytes following 4 hour exposure to mannitol and $Ti_3C_2T_x$. Actin cytoskeletal structure was stained using TRITC conjugated rhodamine phalloidin (red), and nuclei were counterstained using DAPI (blue). Scale bar = 100 μm.

tion (ESI Fig. 8†). As shown in Fig. 7(c), submerging the [*t*Bu-GB]$^+$/[PAA-*co*-EGDMA]$^-$ microgels in aqueous surroundings immediately initiated the elution of both free GB and *t*Bu-GB. The release of GB was approximately linear over the 48 h study period (2.0% h^{-1}, R^2 = 0.995). This is a desirable feature in any drug or therapeutic molecule-releasing system, as it enables accurate dose estimation at any given time following initial administration. Additionally, the persistent release of new GB and *t*Bu-GB, despite the repeated removal and replenishment of aqueous supernatant, indicates that the cross-linked acry-

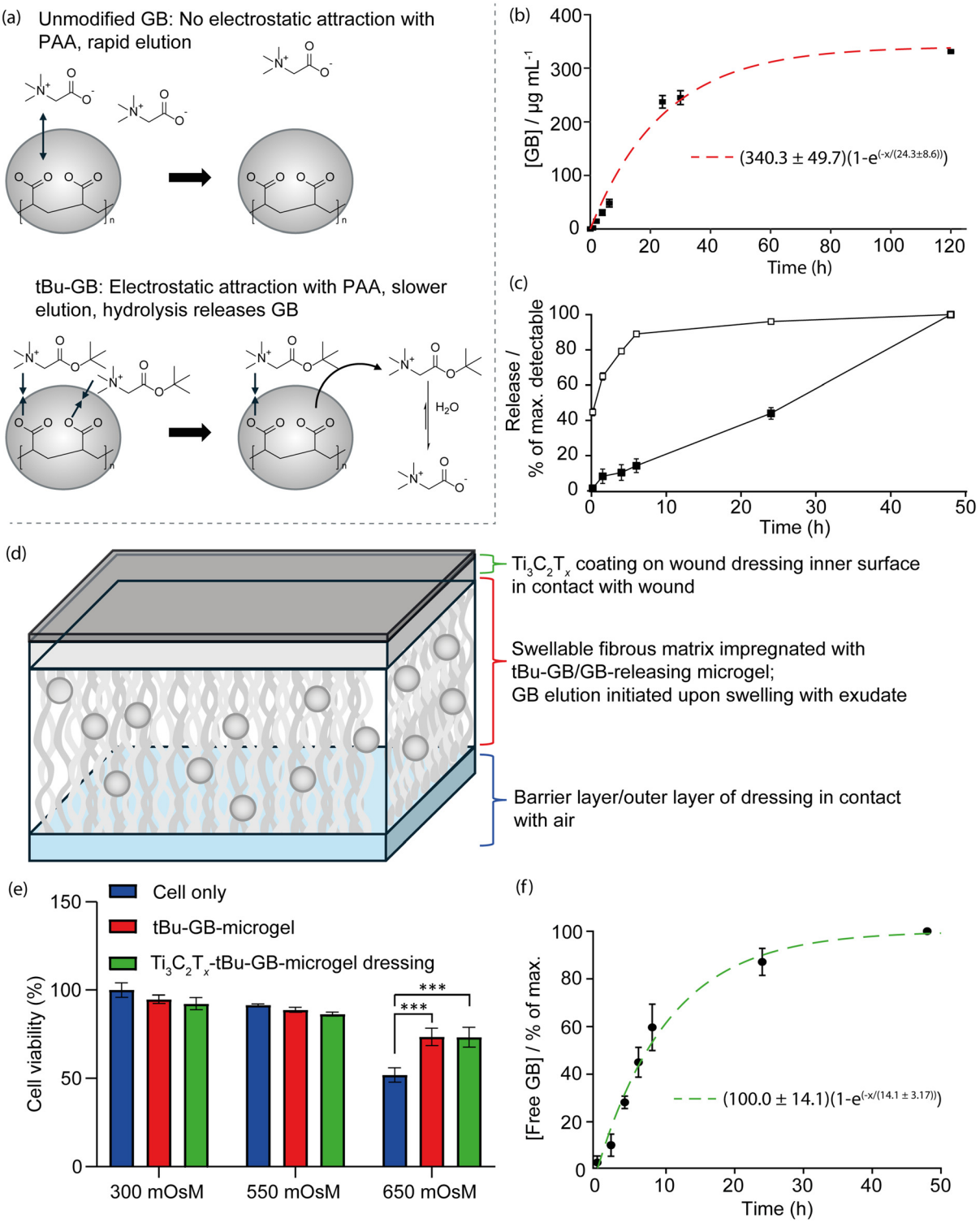

Fig. 7 Synthesis and testing of a $Ti_3C_2T_x$-*t*Bu-GB-microgel wound dressing for slow elution of GB from a *t*Bu-GB impregnated microgel within the dressing over time. (a) Illustration of the GB release mechanism from the acrylate-based PAA microgels. (b) Best fit curve plot showing first-order release of GB from a 2.5 mg mL^{-1} solution of *t*Bu-GB at pH 7.2 in 32 °C PBS, as absolute concentration µg mL^{-1}. (c) Release of free GB (black squares) and *t*Bu-GB (white squares) from [*t*Bu-GB]+/[PAA-co-EGDMA]- microgels in PBS at pH 7.2 at 32 °C, as concentration relative to the maximum concentration detected after 48 h. (d) Schematic of the cross-section of the bioactive wound dressing employing both $Ti_3C_2T_x$ layer and GB elution technologies to enhance the wound healing process. (e) MTS cytotoxicity plot for HaCaT cells incubated with *t*Bu-GB/acrylate microgel-loaded, $Ti_3C_2T_x$-coated dressing under isotonic and hyperosmotic conditions (550 and 650 mOsM) (n = 3, mean ± SEM, ***p < 0.001) (f) Best fit curve plot showing first-order elution of GB from the $Ti_3C_2T_x$-*t*Bu-GB-microgel wound dressing over time.

late gels are effective in entrapping *t*Bu-GB and GB. Interestingly, the release of GB from the gels continues for at least 24 h after no new release of *t*Bu-GB is evident. *t*Bu-GB release is 89% complete within 6 h, yet significant GB release continues between 24–48 h. This may indicate that significant quantities of unreleased *t*Bu-GB remain bound to the gel and do not enter the solution, or hydrolysis of *t*Bu-GB occurs predominantly in/at the gels rather than the aqueous surroundings.

The scratch assay data indicated that the presence of $Ti_3C_2T_x$ and GB at 10 mM in a simulated osmotically challenged non-healing scratch wound increased the scratch closure rate such that the scratch reached 100% closure within 48 h. Thus, from the release data above, the release duration of GB from the *t*Bu-GB-loaded microgels appears suitable for promoting scratch wound closure under osmotically challenged conditions. Over the 48 h study period, 1.75 μg of GB and 31.25 μg *t*Bu-GB were released per mg of microgel material. Assuming 31.25 μg *t*Bu-GB evolves *ca.* 24.9 μg GB (as indicated previously), the total releasable GB is *ca.* 26 μg mg^{-1}. Based on the approximately linear 2.0% h^{-1} release gradient, this is equal to 0.5 μg mg^{-1} h^{-1}. It is likely that the total loading and release profiles can be adjusted by varying the ratio of AA to EGDMA in the system.[66,67]

Following demonstration of a successful encapsulation mechanism by which bioactive osmolyte GB could be incorporated into a $Ti_3C_2T_x$ dressing a $Ti_3C_2T_x$-*t*Bu-GB-microgel dressing was fabricated and tested for biocompatibility and efficacy. The wound dressing was prepared by dispersing dry microgels of *ca.* 10 μm in size in the fibrous absorbent inner layers of the dressing material, designed to absorb and swell with retained wound exudate. The simple and efficient spray-coating method developed in this work, was used to coat the wound-facing surface of the dressing, shown in Fig. 7(d). The therapeutic $Ti_3C_2T_x$ layer would then remain in contact with the wound bed, and the absorption of exudate by the dressing would result in the swelling of the embedded microgels, slowly releasing GB into the wound bed by the mechanisms described in section 3.3. FTIR spectral analysis of the microgels with and without *t*Bu-GB loading in addition to the cellulose based commercial dressing with and without *t*Bu-GB microgel loading and an outer $Ti_3C_2T_x$ coating indicated successful incorporation of each component within the final dressing and is described in ESI Fig. 9.†

The fabricated $Ti_3C_2T_x$-*t*Bu-GB-microgel dressing was assessed for keratocyte cytotoxicity, protective effects against hyperosmotic stress and slow elution of GB over time. Using a 24 h conditioned media study, it was found that the *t*Bu-GB microgel alone and within the $Ti_3C_2T_x$-*t*Bu-GB-microgel dressing, had no effect on cell viability indicating its biocompatibility. This was in agreement with the direct contact cell viability data shown in Fig. 3a for the GB and $Ti_3C_2T_x$ components (Fig. 7(e)). In addition, under hyperosmotic (650 mOsM) conditions, sufficient to significantly reduce cell viability, the *t*Bu-GB-microgel and $Ti_3C_2T_x$-*t*Bu-GB-microgel dressing conditioned media, provided a protective effect, significantly increasing cell viability compared to that of the cell only control. This indicated that slow elution of GB from both the *t*Bu-GB-microgel alone and the $Ti_3C_2T_x$-*t*Bu-GB-microgel dressing into the media was sufficient to then protect the HaCaT cells from osmotic stress induced cell death. The result was confirmed by a slow elution study from the $Ti_3C_2T_x$-*t*Bu-GB-microgel dressing over time indicating the release of free GB from the dressing over a period of 48 h (Fig. 7(f)). A single-term exponential saturation model, given by $M(1 - e^{(-x/T)})$, was fitted to the release curve as shown in Fig. 7f, and based on an R^2 value of 0.9797, this model effectively captures the release kinetics of GB from the microgel dressing. The parameter M represents the total amount of GB that can be released over time, corresponding to the final plateau value in the plot. The coefficient T defines the characteristic time required to reach approximately 63% of the total release. Beyond this point, the release rate slows down, asymptotically approaching 100%, which represents the final equilibrium amount of GB released. A higher T value suggests a more prolonged release due to slower diffusion, whereas a lower T value indicates a faster elution process.

This work aims to engineer a wound dressing that exerts the synergistic therapeutic and anti-inflammatory properties of GB-$Ti_3C_2T_x$ to alleviate hyperosmotic stress and promote a transition from persistent hyper-inflammation to wound healing. This bio-interactive dressing approach also provides the potential for a smart dressing design that would enable release by pathologically raised triggers within the chronic wound bed. There are other examples of this approach within the drug delivery literature, exploiting the body's own interactions with polymer and liposome surface biomolecule conjugates to initiate targeted drug release at specific sites.[68–70]

4. Conclusion

In this study, $Ti_3C_2T_x$ was investigated for use in a bioactive device designed to mitigate the mechanisms active within the chronic wound bed, which lead to poor wound repair. $Ti_3C_2T_x$ was combined with a bioactive osmoprotectant to specifically consider the potential of these materials to protect against the damaging effects of hyperosmotic stress. In the context of wound repair, hyperosmotic stress is an underexplored but potentially significant contributor to inflammation and infection-associated delays in the activation of cellular repair pathways. Whilst normal osmo-adaptive mechanisms exist to regulate any osmotic flux within physiological limits, chronic shifts linked to systemic disease can disrupt this balance to provoke damage to the wound bed environment and prevent wound closure. This study showed that the ability of dermal keratocytes to close a scratch wound was prevented under mannitol-induced hyperosmotic stress conditions and that $Ti_3C_2T_x$ could reverse this effect to allow wound closure. $Ti_3C_2T_x$ coatings significantly increased the rate and velocity of keratocyte migration to close the scratch wound. This protective effect was increased by including osmoprotectant GB, demonstrating

a synergistic effect of the $Ti_3C_2T_x$ coating with this bioactive molecule. The same effect was demonstrated on measuring inflammatory pathway upregulation by migratory keratocytes. Hyperosmotic stress-induced upregulation of IL-6, IL-1α, IL-1β, CXCL1, and CXCL8, and this effect was primed by pre-incubation of keratocytes with bacterial LPS to further increase inflammatory cytokine and chemokine upregulation. $Ti_3C_2T_x$ was able to significantly reduce the production of these inflammatory markers towards that of the non-stressed, cell-only control in the presence and absence of bacterial LPS. The effect was augmented by the presence of GB, again suggesting a synergistic role for these materials. $Ti_3C_2T_x$ demonstrated a protective effect towards apoptotic stimuli and oxidative stressors, in addition to preventing osmotic stress induced cytoskeletal changes. The study also presents a slow elution mechanism by which GB may be released into the wound bed within a bioactive $Ti_3C_2T_x$ dressing in a tissue engineering approach to repress inflammation and oxidative stress and improve migratory stimulus for chronic wound repair.

Author contributions

SK, EJW, DH, AS and SS were responsible for the conceptualisation, implementation, planning, writing and revision of the paper. SK, DH and AS carried out the experimental and mathematical modelling work. SS, DH, AS, DS and CC supervised the work of SK. GC, CC, AL, CS and YG provided conceptual input, critical feedback and comments for draft writing and improvement.

Data availability

The data supporting this article have been included as part of the ESI.†

Conflicts of interest

There are no conflicts to declare.

Acknowledgements

University of Brighton authors acknowledge the EPSRC grant MyDress (EP/W023164/1). XRD was carried out by Prof. Martin Smith at the University of Brighton.

References

1 J. F. Guest, G. W. Fuller and P. Vowden, *BMJ Open*, 2020, **10**, e045253.
2 H. Deng, B. Li, Q. Shen, C. Zhang, L. Kuang, R. Chen, S. Wang, Z. Ma and G. Li, *J. Diabetes*, 2023, **15**, 299–312.
3 M. J. Portou, R. Yu, D. Baker, S. Xu, D. Abraham and J. Tsui, *Eur. J. Vasc. Endovasc. Surg.*, 2020, **59**, 117–127.
4 Q. Pang, F. Yang, Z. Jiang, K. Wu, R. Hou and Y. Zhu, *Mater. Des.*, 2023, **229**, 111917.
5 P. Alves, C. Barrias, P. Gomes and M. Martins, *Mater. Today Chem.*, 2021, **22**, 100623.
6 Y. Hu, F. Wang, H. Ye, J. Jiang, S. Li, B. Dai, J. Li, J. Yang, X. Song and J. Zhang, *npj Flexible Electron.*, 2024, **8**, 30.
7 E. Bachar-Wikstrom, M. Manchanda, R. Bansal, M. Karlsson, P. Kelly-Pettersson, O. Sköldenberg and J. D. Wikstrom, *Int. Wound J.*, 2021, **18**, 49–61.
8 S. Akita, *Int. J. Mol. Sci.*, 2019, **20**, 6328.
9 H. N. Wilkinson and M. J. Hardman, *Open Biol.*, 2020, **10**, 200223.
10 P. Rousselle, F. Braye and G. Dayan, *Adv. Drug Delivery Rev.*, 2019, **146**, 344–365.
11 U. A. Okonkwo and L. A. DiPietro, *Int. J. Mol. Sci.*, 2017, **18**, 1419.
12 P. Lu, D. Ruan, M. Huang, M. Tian, K. Zhu, Z. Gan and Z. Xiao, *Signal Transduction Targeted Ther.*, 2024, **9**, 166.
13 D. V. Verdolino, H. A. Thomason, A. Fotticchia and S. Cartmell, *Emerging Top. Life Sci.*, 2021, **5**, 523–537.
14 R. Dong and B. Guo, *Nano Today*, 2021, **41**, 101290.
15 G. Zhao, F. Liu, Z. Liu, K. Zuo, B. Wang, Y. Zhang, X. Han, A. Lian, Y. Wang and M. Liu, *Stem Cell Res. Ther.*, 2020, **11**, 1–18.
16 Z. Xu, S. Han, Z. Gu and J. Wu, *Adv. Healthcare Mater.*, 2020, **9**, 1901502.
17 A. Hautmann, D. Kedilaya, S. Stojanović, M. Radenković, C. K. Marx, S. Najman, M. Pietzsch, J. F. Mano and T. Groth, *Biomater. Adv.*, 2022, **142**, 213166.
18 S. Obuobi, H. K.-L. Tay, N. D. T. Tram, V. Selvarajan, J. S. Khara, Y. Wang and P. L. R. Ee, *J. Controlled Release*, 2019, **313**, 120–130.
19 S. Gera, E. Kankuri and K. Kogermann, *Pharmacol. Ther.*, 2022, **232**, 107990.
20 C.-F. Hsieh, C.-H. Chen, H.-H. Kao, D. T. Govindaraju, B. S. Dash and J.-P. Chen, *Biomedicines*, 2022, **11**, 2902.
21 X. Lin, B. Kong, Y. Zhu and Y. Zhao, *Adv. Sci.*, 2022, **9**, 2201226.
22 J. Franková, V. Pivodová, H. Vágnerová, J. Juráňová and J. Ulrichová, *J. Appl. Biomater. Funct. Mater.*, 2016, **14**, 137–142.
23 C. You, Q. Li, X. Wang, P. Wu, J. K. Ho, R. Jin, L. Zhang, H. Shao and C. Han, *Sci. Rep.*, 2017, **7**, 10489.
24 H. Hanif, G. Sanjay, Z. K. Vasilev and J. C. Allison, *Wound Pract. Res.*, 2020, **28**, 173–180.
25 G. Cooksley, M. K. Dymond, N. A. Stewart, G. Bucca, A. Hesketh, J. Lacey, Y. Gogotsi and S. Sandeman, *2D Mater.*, 2022, **10**, 014003.
26 T. Ozulumba, G. Ingavle, Y. Gogotsi and S. Sandeman, *Biomater. Sci.*, 2021, **9**, 1805–1815.
27 A. Zarepour, N. Rafati, A. Khosravi, N. Rabiee, S. Iravani and A. Zarrabi, *Nanoscale Adv.*, 2024, **6**, 3513–3532.

28 E. J. Ward, J. Lacey, C. Crua, M. K. Dymond, K. Maleski, K. Hantanasirisakul, Y. Gogotsi and S. Sandeman, *Adv. Funct. Mater.*, 2020, **30**, 2000841.
29 Y. Li, R. Fu, Z. Duan, C. Zhu and D. Fan, *ACS Nano*, 2022, **16**, 7486–7502.
30 E. K. Hoffmann, I. H. Lambert and S. F. Pedersen, *Physiol. Rev.*, 2009, **89**, 193–277.
31 S. A. Craig, *Am. J. Clin. Nutr.*, 2004, **80**, 539–549.
32 S. A. Kempson, Y. Zhou and N. C. Danbolt, *Front. Physiol.*, 2014, **5**, 159.
33 S. M. Hosseiniyan Khatibi, F. Zununi Vahed, S. Sharifi, M. Ardalan, M. Mohajel Shoja and S. Zununi Vahed, *Biochimie*, 2019, **158**, 156–164.
34 M. K. Arumugam, M. C. Paal, T. M. Donohue Jr, M. Ganesan, N. A. Osna and K. K. Kharbanda, *Biology*, 2021, **10**, 456.
35 M. Bhatt, A. Di Iacovo, T. Romanazzi, C. Roseti and E. Bossi, *Basic Clin. Pharmacol. Toxicol.*, 2023, **133**, 485–495.
36 L. S. Knight, Q. Piibe, I. Lambie, C. Perkins and P. H. Yancey, *Neurochem. Res.*, 2017, **42**, 3490–3503.
37 C. R. Day and S. A. Kempson, *Biochim. Biophys. Acta*, 2016, **1860**, 1098–1106.
38 X. Hua, Z. Su, R. Deng, J. Lin, D.-Q. Li and S. C. Pflugfelder, *Curr. Eye Res.*, 2015, **40**, 657–667.
39 K.-H. Hsu, P. Lazon de la Jara, A. Ariyavidana, J. Watling, B. Holden, Q. Garrett and A. Chauhan, *Curr. Eye Res.*, 2015, **40**, 267–273.
40 J. J. López-Cano, M. A. González-Cela-Casamayor, V. Andrés-Guerrero, R. Herrero-Vanrell, J. M. Benítez-Del-Castillo and I. T. Molina-Martínez, *Exp. Eye Res.*, 2021, **211**, 108723.
41 C. El-Chami, A. R. Foster, C. Johnson, R. P. Clausen, P. Cornwell, I. S. Haslam, M. C. Steward, R. E. B. Watson, H. S. Young and C. A. O'Neill, *Br. J. Dermatol.*, 2021, **184**, 482–494.
42 C. Brocker, D. C. Thompson and V. Vasiliou, *Biomol. Concepts*, 2012, **3**, 345–364.
43 M. Alhabeb, K. Maleski, B. Anasori, P. Lelyukh, L. Clark, S. Sin and Y. Gogotsi, *Chem. Mater.*, 2017, **29**, 7633–7644.
44 C. E. Shuck, A. Sarycheva, M. Anayee, A. Levitt, Y. Zhu, S. Uzun, V. Balitskiy, V. Zahorodna, O. Gogotsi and Y. Gogotsi, in *MXenes*, Jenny Stanford Publishing, 2023, pp. 539–560.
45 M. Tabatabai, D. K. Williams and Z. Bursac, *Theor. Biol. Med. Modell.*, 2005, **2**, 1–13.
46 M. Shekhirev, C. E. Shuck, A. Sarycheva and Y. Gogotsi, *Prog. Mater. Sci.*, 2021, **120**, 100757.
47 W. Chen, X. Zhang, J. Li, Y. Wang, Q. Chen, C. Hou and Q. Garrett, *Invest. Ophthalmol. Visual Sci.*, 2013, **54**, 6287–6297.
48 F. Ascione, A. Vasaturo, S. Caserta, V. D'Esposito, P. Formisano and S. Guido, *Exp. Cell Res.*, 2016, **347**, 123–132.
49 H. Li, M. Mu, B. Chen, L. Zhou, B. Han and G. Guo, *Mater. Res. Lett.*, 2024, **12**, 67–87.
50 J. Yang, N. Cai, H. Zhai, J. Zhang, Y. Zhu and L. Zhang, *Sci. Rep.*, 2016, **6**, 37458.
51 P. G. Petronini, E. De Angelis, P. Borghetti, A. Borghetti and K. P. Wheeler, *Biochem. J.*, 1992, **282**, 69–73.
52 M. D'Souza-Ault, L. T. Smith and G. Smith, *Appl. Environ. Microbiol.*, 1993, **59**, 473–478.
53 A. Sakamoto and N. Murata, *Plant, Cell Environ.*, 2002, **25**, 163–171.
54 M. Ashraf and M. R. Foolad, *Environ. Exp. Bot.*, 2007, **59**, 206–216.
55 A. Bonaterra, J. Camps and E. Montesinos, *FEMS Microbiol. Lett.*, 2005, **250**, 1–8.
56 G. Zhao, F. He, C. Wu, P. Li, N. Li, J. Deng, G. Zhu, W. Ren and Y. Peng, *Front. Immunol.*, 2018, **9**, 1070.
57 M. Veskovic, D. Mladenovic, M. Milenkovic, J. Tosic, S. Borozan, K. Gopcevic, M. Labudovic-Borovic, V. Dragutinovic, D. Vucevic and B. Jorgacevic, *Eur. J. Pharmacol.*, 2019, **848**, 39–48.
58 C.-Y. Fan, M.-X. Wang, C.-X. Ge, X. Wang, J.-M. Li and L.-D. Kong, *J. Nutr. Biochem.*, 2014, **25**, 353–362.
59 Y. He, H. Sun, Y. Wang, C. Mu and L. Chen, *Chem. Eng. J.*, 2024, **485**, 150047.
60 H. Geng, Y. Ren, G. Qin, T. Wen, Q. Liu, H. Xu and W. He, *RSC Adv.*, 2022, **12**, 11128–11138.
61 L. Hou, F. Gong, B. Liu, X. Yang, L. Chen, G. Li, Y. Gong, C. Liang, N. Yang and X. Shen, *Theranostics*, 2022, **12**, 3834.
62 M. A. Velazco-Medel, L. A. Camacho-Cruz and E. Bucio, *Radiat. Phys. Chem.*, 2020, **171**, 108754.
63 A. Tuncel, K. Ecevit, K. Kesenci and E. Pişkin, *J. Polym. Sci., Part A: Polym. Chem.*, 1996, **34**, 45–55.
64 T. Hoare and R. Pelton, *Langmuir*, 2008, **24**, 1005–1012.
65 S. W. Kim, Y. H. Bae and T. Okano, *Pharm. Res.*, 1992, **9**, 283–290.
66 B. Lu, M. Tarn, N. Pamme and T. Georgiou, *J. Mater. Chem. B*, 2015, **3**, 4524–4529.
67 T.-L. Tsou, S.-T. Tang, Y.-C. Huang, J.-R. Wu, J.-J. Young and H.-J. Wang, *J. Mater. Sci.: Mater. Med.*, 2005, **16**, 95–100.
68 M. T. Manzari, Y. Shamay, H. Kiguchi, N. Rosen, M. Scaltriti and D. A. Heller, *Nat. Rev. Mater.*, 2021, **6**, 351–370.
69 A. Tewabe, A. Abate, M. Tamrie, A. Seyfu and E. Abdela Siraj, *J. Multidiscip. Healthcare*, 2021, 1711–1724.
70 Y. Li, C. Zhang, G. Li, G. Deng, H. Zhang, Y. Sun and F. An, *Acta Pharm. Sin. B*, 2021, **11**, 2220–2242.